

Generating Mock Catalogs for the Baryon Oscillation Spectroscopic Survey: An Approximate N-Body approach

Tomomi Sunayama^a, Nikhil Padmanabhan^a, Katrin Heitmann^b,
Salman Habib^b, Steve Rangel^{b,c}

^aYale University, New Haven, CT

^bArgonne National Laboratory, Lemont, IL

^cNorthwestern University, Evanston, IL

E-mail: tomomi.sunayama@yale.edu, nikhil.padmanabhan@yale.edu, heitmann@anl.gov,
habib@anl.gov, steverangel@u.northwestern.edu

Abstract. Precision large scale structure measurements require large numbers of mock catalogs of high fidelity to accurately assess the levels of systematic effects. We introduce and test an approximate scheme for generating mock catalogs rapidly. Our aim here is to reproduce the large scale structure and the gross properties of dark matter halos with high accuracy while sacrificing the details of the internal structures of halos for speed. Our N-body code splits the evolution into global time steps for the long range force interleaved with a number of sub-cycles for the short range forces. By adjusting both of these, we demonstrate recover the large scale probes we consider, including individual halo masses to better than 2% and the power spectrum to $k = 1h^{-1}\text{Mpc}$ to better than 1%, while requiring a factor of 4 less CPU time. We also test the redshift spacing of outputs required to generate light cone outputs. We find that $\Delta z = 0.05$ outputs allow us to interpolate particle positions and velocities with sufficient accuracy to reproduce the real and redshift space power spectra to better than 1% (out to $k = 1h^{-1}\text{Mpc}$). Even with redshift spacing as large as $\Delta z = 0.25$, these errors only degrade on less than 2% in both real and redshift spaces. As a demonstration of these ideas, we generate a suit of simulations matched to the Baryon Oscillation Spectroscopic sample.

Keywords: cosmology; large-scale structure of Universe, cosmological parameters, galaxies; halos, statistics

Contents

1	Introduction	1
2	HACC	2
3	Convergence Test: Selection of the minimal time steps	3
3.1	Matching	3
3.1.1	Algorithm	3
3.1.2	Halo Properties	5
3.2	Mass Adjustment	6
3.2.1	Method	7
3.2.2	Observables	8
4	Constructing Light Cones	9
5	THE BOSS SIMULATIONS	12
5.1	Building the Galaxy Catalog	13
6	Discussion	15

1 Introduction

Recently, the necessity and the demand for the large number of large N-body simulations have been increased in astronomy due to the precision required for measurements to understand cosmic acceleration, like the Baryon Oscillation Spectroscopic Survey (BOSS) and the proposed Mid Scale-Dark Energy Spectroscopic Instrument (MS-DESI). As the area covered by those current and future spectroscopic galaxy surveys get larger, galaxy mocks necessary to the cosmological analysis also have to be generated from N-body simulations with the corresponding large volume, which is computationally expensive. Many studies have been done recently on the implementation of large N-body simulations [1–12]. Besides the large volume required for the N-body simulations, we need many realizations to achieve the precision required for those measurements.

One of the simplest adjustments to an N-body simulation is to adjust the length of each individual time step. This is the approach taken in [6, 7]; indeed, the 2LPT mock simulations of [13, 14] are an extreme version of this. These works have focused on relatively small numbers of time steps, accurately capturing the large scale density field, but losing information on small scales. While such approaches are invaluable for generating the large numbers of simulations required to build sample covariance matrices, it is harder to quantify the impact of the loss of accuracy on systematic tests. Our N-body simulations consist of two components: a long time step for solving the PM force and a set of short range sub-cycle steps for a direct particle-particle interaction. The idea behind is reducing the number of both time steps as much as we can preserve enough mass resolution to correctly describe the large scale distribution of galaxies. Our first goal in this paper is to work at a different end of the spectrum : we aim to accurately reproduce the details of the halo density field on large scales, sacrificing the small scale structure with large time steps. Our second goal, is to build a suite of simulations and related mock catalogs suitable for the Baryon Oscillation Spectroscopic Survey galaxy samples. These both serve as a demonstration of our approach, but will be useful for evaluating systematic errors in these surveys.

In the following, we first briefly describe the mechanism of our approximated N-body simulations. In Section 3, we test and compare our method to the full N-body simulation and explain how we calibrate our samples. In Section 4 and 5, we build a light cone output and populate halos in our samples with galaxies and compute correlation functions based on BOSS Data Release 11, and compare it with the observed correlation function.

All simulations and calculations in this paper assume a Λ CDM cosmology with $\Omega_m = 0.2648$, $\Omega_\Lambda = 0.7352$, $\Omega_b h^2 = 0.02258$, $n_s = 0.963$, $\sigma_8 = 0.8$ and $h = 0.71$.

2 HACC

All simulations in this paper were carried out using the HACC (Hardware/Hybrid Accelerated Cosmology Code) framework. HACC provides an advanced, architecture-agile, extreme-scale N-body capability targeted to cosmological simulations. It is descended from an approach originally developed for the heterogeneous architecture of Roadrunner [15, 16], the first computer to break the petaflop performance barrier.

The HACC architecture is designed with great flexibility in mind (combining MPI with a variety of more local programming models, e.g., OpenCL, OpenMP) and is easily adaptable to different platforms. Currently, it is implemented on Cell-accelerated hardware, conventional and GPU-enhanced clusters (via OpenCL), on the IBM Blue Gene architecture (using OpenMP), and is running on prototype Intel MIC/Xeon Phi hardware. HACC is the first, and currently the only large-scale cosmology code suite world-wide, that can run at full scale on all available supercomputer architectures, at very high performance levels. HACC has demonstrated scaling on the entire IBM BG/Q Sequoia system up to 1,572,864 cores with an equal number of MPI ranks, attaining 13.94 PFlops at 69.2% of peak and 90% parallel efficiency (for details, see Ref.[17]). Examples of science results obtained using HACC include 64-billion particle runs for baryon acoustic oscillations predictions for the BOSS Lyman- α forest [18] and high-statistics predictions for the halo profiles of massive clusters [19].

HACC uses a hybrid parallel algorithmic structure, splitting the force calculation into a specially designed grid-based long/medium range spectral particle-mesh (PM) component that is common to all architectures, and an architecture-specific short-range solver. Modular code design combined with particle caching allows the short-range solvers to be ‘hot-swappable’ on-node; they are blind to the parallel implementation of the long-range solver. The short-range solvers can use direct particle-particle interactions, i.e., a P³M algorithm [20], as on (Cell or GPU) accelerated systems, or use tree methods on conventional or many-core architectures. (This was the case for the simulations reported here.) In all cases, the time-stepping scheme is based on a symplectic method with (adaptive) sub-cycling of the short-range force. The availability of multiple algorithms within the HACC framework allows us to carry out careful error analyses, for example, the P³M and the TreePM versions agree to within 0.1% for the nonlinear power spectrum test in the code comparison suite of Ref. [21].

An important feature of the work proposed here is the ability to carry out error-controlled approximate simulations at high throughput. In order to understand how we implement this, some details of the HACC time-stepping algorithm are now provided. Evolution is viewed as a symplectic map on phase space: $\zeta(t) = \exp(-t\mathbf{H})\zeta(0)$ where, ζ is a phase-space vector (\mathbf{x}, \mathbf{v}) , H is the (self-consistent) Hamiltonian, and the operator, $\mathbf{H} = [H, \]_P$, denotes the action of taking the Poisson bracket with the Hamiltonian. Suppose that the Hamiltonian can be written as the sum of two parts; then by using the Campbell-Baker-Hausdorff (CBH) series we can build an integrator for the time evolution; repeated application of the CBH formula yields

$$\exp(-t(\mathbf{H}_1 + \mathbf{H}_2)) = \exp(-(t/2)\mathbf{H}_1) \exp(-t\mathbf{H}_2) \exp(-(t/2)\mathbf{H}_1) + O(t^3),$$

a second order symplectic integrator. In the basic PM application, the Hamiltonian H_1 is the free particle (kinetic) piece while H_2 is the one-particle effective potential; corresponding respectively to the ‘stream’ and ‘kick’ maps $M_1 = \exp(-t\mathbf{H}_1)$ and $M_2 = \exp(-t\mathbf{H}_2)$. In the stream map, the particle position is drifted using its known velocity, which remains unchanged; in the kick map, the velocity is updated using the force evaluation, while the position remains unchanged. This symmetric ‘split-operator’ step is termed SKS (stream-kick-stream). A KSK scheme constitutes an alternative second-order symplectic integrator.

In the presence of both short and long-range forces, we split the Hamiltonian into two parts, $H_1 = H_{sr} + H_{lr}$ where H_{sr} contains the kinetic and particle-particle force interaction (with an associated map M_{sr}), whereas, $H_2 = H_{lr}$ is just the long range force, corresponding to the map

M_{lr} . Since the long range force varies relatively slowly, we construct a single time-step map by sub-cycling M_{sr} : $M_{full}(t) = M_{lr}(t/2)(M_{sr}(t/n_c))^{n_c} M_{lr}(t/2)$, the total map being a usual second-order symplectic integrator. This corresponds to a KSK step, where the S is not an exact stream step, but has enough M_{sr} steps composed together to obtain the required accuracy. (We take care that the time-dependence in the self-consistent potential is treated correctly.) As discussed later below, we will use the flexibility in the sub-cycling as a way of reducing the number of time steps such that the loss of accuracy only affects the resolution at very small scales, which, as discussed previously, are not of interest in the current set of simulations.

3 Convergence Test: Selection of the minimal time steps

In this section, we examine how reducing the number of time steps affects halo properties (i.e., halo mass, position, and velocity), as well as observables such as halo mass functions and halo bias. In order to quantitatively evaluate different time-stepping options, we run a set of convergence tests with down-scaled simulation boxes, using simulation volumes of size $(256h^{-1}\text{Mpc})^3$ and 256^3 particles. These runs have the same particle mass as the main $(4000h^{-1}\text{Mpc})^3$ volume simulations.

Time-stepping convergence was studied using the following time step options: 450/5, 300/3, 300/2, 150/3, and 150/2, where the first number indicates the number of long time steps and the second number the number of short sub-time steps for each long time step. To evaluate the different time-stepping options, we first compare the properties (masses, positions, and velocities) of individual halos by matching halos in one simulation run to halos in another, using identical initial conditions, and with adaptive time-stepping switched off. Following this, we compare statistical descriptions such as halo mass functions and density power spectra. We found that, for the purpose of the work presented in this paper, differences in halo properties do not significantly affect the statistical observables. Based on a number of convergence tests, the 300/2 time-stepping option was found sufficient to resolve the positions and masses of halos reliably.

3.1 Matching

In order to compare detailed halo properties we need to match individual halos across different runs. We first discuss the algorithm used for identifying the corresponding halos in the two cases and then compare halo mass, position, and velocity for the matched halos. From this quantitative comparison, we find that the simulations with 300 global time steps have significantly less scatter in the measured quantities, compared to the baseline determined by the 450/5 simulation, than do the samples with 150 global steps. In addition, we find that the differences between the different sub-cycling choices are almost negligible.

3.1.1 Algorithm

All the simulations start with the same particle initial conditions, therefore we match halos in different runs by matching their particle content, using individual particle identification. Given a halo in simulation A, we consider halos in simulation B that between them hold all the particles belonging to the halo in simulation A. Given this list of possible matches, we choose the run B halo with the largest number of common particles with the reference halo in run A. To avoid spurious matches, we also require that the fraction of common particles (relative to simulation A) exceeds a given threshold. To illustrate how this matching algorithm works, we use the samples from the 300/2 simulation and the 450/5 simulation, and adopt a threshold of 50% as our default choice. (Figure 2 demonstrates that the unmatched fraction increases with increasing threshold and decreasing halo mass.)

The matching algorithm described above is unidirectional, hence multiple halos in run A may have particles resident in a single halo in run B; in our simulations, this happens at the 1-2% level, adopting a particle matching threshold of 50%. We refer to these cases as ‘multiply-booked’ halos. Figure 1 compares halo masses matching the 450/5 simulation to the 300/2 simulation for the case of multiply-booked halos as well as the rest. The top left panel shows the mass scatter for all the matched halos between the two simulations, while the top right panel shows the mass scatter only for the non multiply-booked halos. The bottom panels show the mass scatter for the case of multiply-booked

halos only. The bottom left panel shows the mass scatter for individual multiply-booked halos, while the bottom right panel plots the summed halo mass for the corresponding halos. The overall behavior represented in Figure 1 is straightforward to interpret.

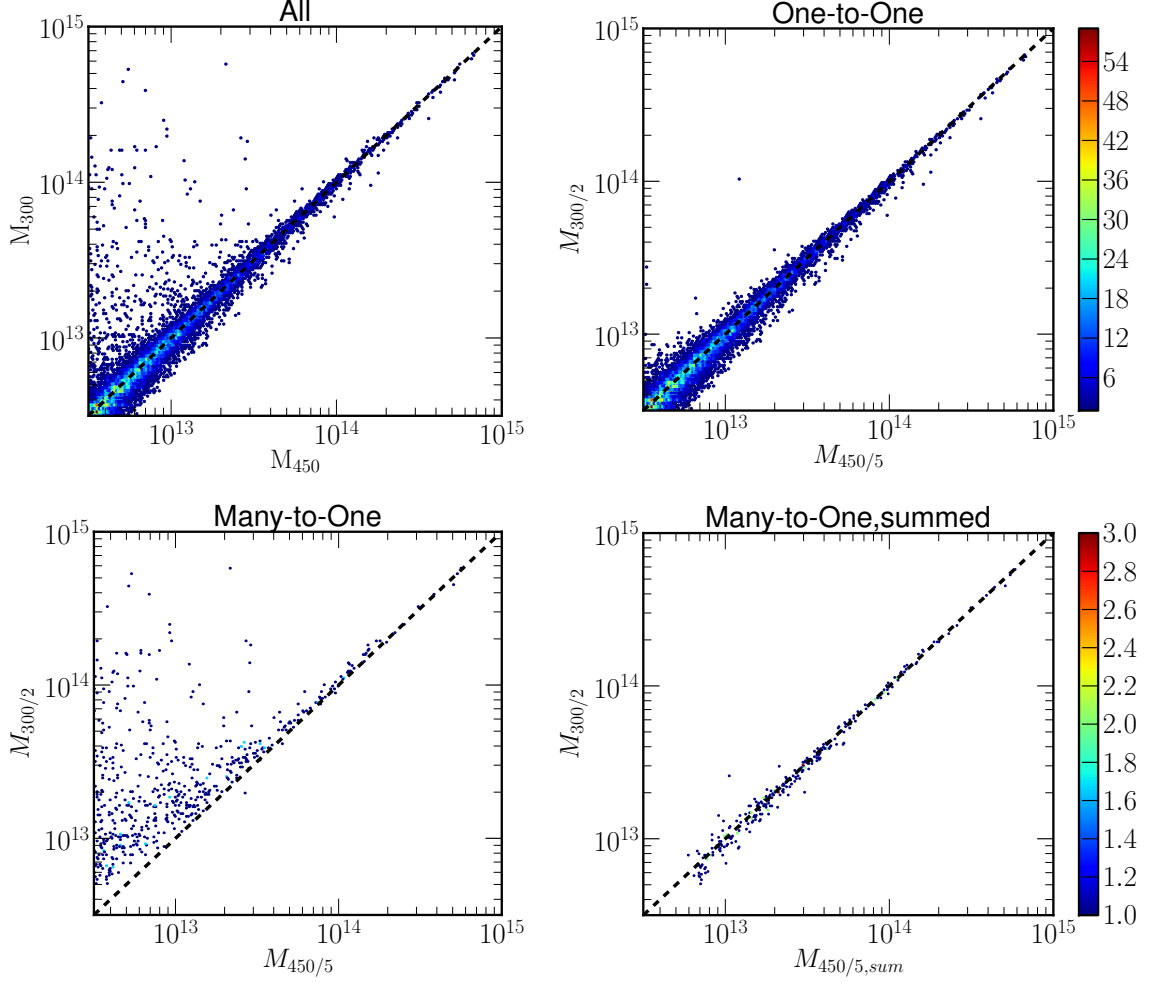


Figure 1. Distribution of halo masses comparing matched halos in the 450/5 simulation (x-axis) to the 300/2 simulation (y-axis) at $z = 0.15$. Panels correspond to halos with different matching criteria imposed: all the matched halos (top left), the vast majority of matched halos having one-to-one correspondence (top right), matched halos not having one-to-one correspondence called “multiply-booked” halos (bottom left), and the “multiply-booked” halos whose corresponding halo masses are added (bottom right). The results shown in these panels imply that the low-mass scatter between the 450/5 simulation and the 300/2 simulation shown in the top left panel arises when “multiply-booked” halos in the 450/5 simulation are merged into one halo in the 300/2 simulation due to an effectively worse resolution in this case.

As the top left panel shows, there are low-mass halos in the 450/5 simulation corresponding to high-mass halos in the 300/2 simulation. The same trend is observed for the case of multiply-booked halos (bottom left panel), but not for the non multiply-booked halos (top right). Furthermore, the disagreement for halo masses between the two simulations are resolved by adding the corresponding halo masses. This implies that there are multiple halos in the 450/5 simulation which are merged into one halo in the 300/2 simulation. The smaller number of time steps in the 300/2 simulations reduces substructure and as well as the compactness of the halos in the 450/5 simulation. Thus, for a small fraction of halos in the 450/5 simulation, individual halos can be merged into a single halo in the 300/2 simulation.

Figure 2 shows the number densities of the unmatched halos in the 450/5 simulation when compared to the 300/2 simulation at $z = 0.15$. There are three reasons that halos can turn up as unmatched. In the first case, particles forming a halo in simulation A may not form a component of a halo in simulation B (no common particles). Second, if the fraction of common particles over the total number of particles in each halo is less than the threshold of 50%, these halos will be eliminated from the matching set. Finally, for the case of multiply-booked halos, we remove all but the one with the largest number of common particles. In Figure 2, we show each type of unmatched number density as a function of halo mass. The first case occurs only for low halo masses, where low effective resolution in a simulation can lead to halo drop out (halos are too ‘fuzzy’ to meet the FOF overdensity criterion), and falls off steeply with rising halo mass. Most of the unmatched halos arise due to their not passing the threshold criterion. The loss of matching due to multiple-booking follows the trend of the below-threshold case, but at a reduced level. We have checked that the trends discussed here are not affected by redshift.

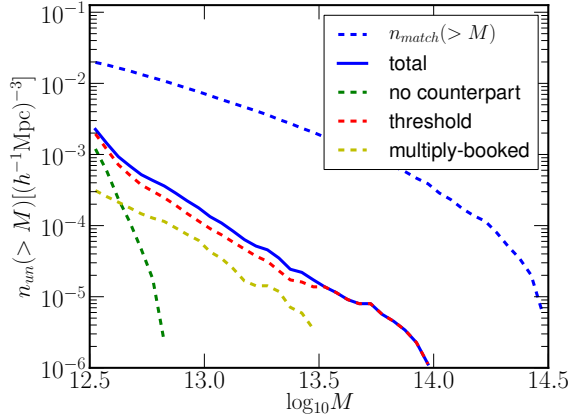


Figure 2. Itemization of unmatched halos (from the 450/5 and 300/2 simulations at $z = 0.15$) shown as cumulative number densities of the unmatched halos arising from each procedure in the matching algorithm. The solid blue line is the total number density of the unmatched halos. The dashed green line shows halos with no counterpart – none of the particles were identified as belonging to a halo in the comparison simulation; this is significant only at low halo mass. The dashed red line shows halos eliminated because of not meeting the matching threshold (i.e., the halos do not have enough of a fraction of the same particles). The dashed cyan line is for the halos eliminated because multiple halos correspond to one halo.

3.1.2 Halo Properties

We now compare halo properties (i.e., halo mass, position, and velocity) for the 300/2 halos that were successfully matched to those in the 450/5 simulation. We are interested in correctly describing the large-scale distribution of galaxies; in the current context, this requires that dark matter halo locations and masses be estimated sufficiently accurately. Therefore, it is essential to systematically investigate the effect of reducing the number of time steps on halo properties.

The comparison of halo mass for different time-stepping schemes to the 450/5 simulation at $z = 0.15$ is shown in Figure 3. We take all the matched halos whose masses are between $10^{12.5}M_{\odot}$ to $10^{13.0}M_{\odot}$, $10^{13.0}M_{\odot}$ to $10^{13.5}M_{\odot}$, and $10^{13.5}M_{\odot}$ to $10^{14.0}M_{\odot}$, and compute their means and standard deviations for $\log_{10}(M/M_{450/5})$, where $M_{450/5}$ is a halo mass for the 450/5 simulation and M corresponds to a halo in the samples generated with different time-stepping schemes. Figure 3 shows that halos generated from the simulations with small number of time steps have systematically lower FOF masses than those in the 450/5 simulation. (The same linking length ($b = 0.168$) is used in the FOF algorithm to define halos for all the simulations.) As stated earlier, reducing the number of time steps produces halos with less substructure and a more diffuse distribution of mass, thus in a direct one-on-one halo comparison, one expects the FOF mass to be highest in the 450/5 simulation, as borne out in the data.

Figure 4 shows the differences in positions (left panel) and velocities (right panel) along x-axis for the matched halos at $z = 0.15$. The simulations with a smaller number of global time steps (150) display significantly more scatter; they also show a small bias in the speed. With 300 global time steps, the results are significantly improved; the velocity bias is almost entirely removed and the scatter is significantly reduced. The standard deviation in the differences in halo distances is matched in these cases to better than $200h^{-1}\text{kpc}$. The dashed lines represent the result from the simulations, while the solid lines are the Gaussian fits, where the values for amplitude, expected value and variance are shown in Table 1. Figure 4 shows that the distribution of the differences in positions and velocities are almost Gaussian. As is clear from Figure 4, the difference between 3 and 2 sub-cycles is negligible on halo properties. Note that we observe the same trend in halo properties discussed here at different redshifts and along different axes.

As shown in Figure 2, the fraction of unmatched halos in the 300/2 simulation to the 450/5 simulation is less than 5% on most of halo mass ranges, which implies that the 300/2 simulation has almost the same number of halos as in the 450/5 simulation. Furthermore, Figure 1 shows that the halo masses in the 450/5 and 300/2 simulations have linear relation with the slope being one. So, most of halos in the 300/2 simulation have the same mass as the ones in the 450/5 simulation. Since the number of sub-cycles do not affect to halo positions and velocities as shown in Figure 4, the 300/2 time step is our choice to save the simulation time while keeping the halo properties almost identical to the 450/5 simulation.

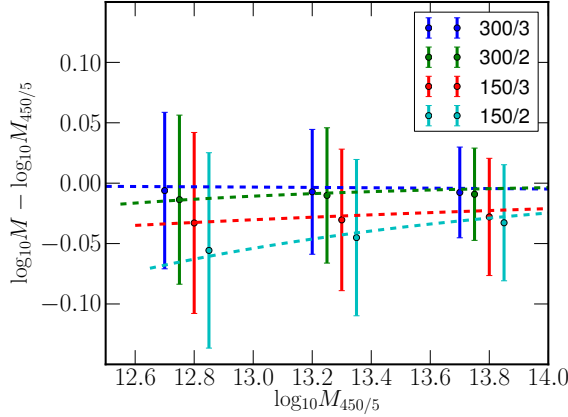


Figure 3. Comparison of halo mass for matched halos between the 450/5 simulation and other time-stepping schemes at $z = 0.15$. We take all the matched halos whose masses are between $10^{12.5}M_{\odot}$ to $10^{13.0}M_{\odot}$, $10^{13.0}M_{\odot}$ to $10^{13.5}M_{\odot}$, and $10^{13.5}M_{\odot}$ to $10^{14.0}M_{\odot}$, and compute the mean and the standard deviation for $\log_{10}(M/M_{450/5})$ where $M_{450/5}$ is a halo mass for the 450/5 simulation and M is for the simulations with different number of time steps corresponding to different colors in the plot. The x-positions of the points have been displaced to avoid overlapping the error bars. This plot shows that halo masses become systematically smaller for the case of smaller numbers of time steps than those in the 450/5 simulation.

3.2 Mass Adjustment

In the previous subsection, Figure 3 shows that halos generated by the de-tuned simulations have systematically lower masses than the halos in the 450/5 simulation. This suggests the necessity of adjusting halo masses for those cases to the halo masses in the 450/5 simulation. In the following, we describe how we do a mass adjustment and show the resulting observables including mass functions and power spectra.

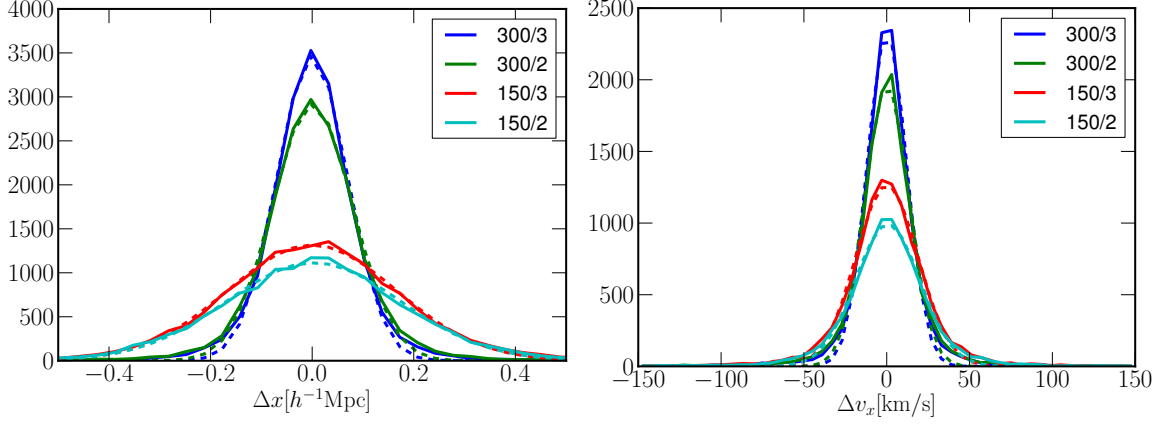


Figure 4. A comparison of the positions [left] and velocities [right] of halos matched across simulations with different time steps. As always, the reference simulation is 450/5 while the colors correspond to 300/3 (blue), 300/2 (green), 150/3 (red), and 150/2 (cyan). From left to right, we compared halo position and velocity respectively. The agreement with 300 time steps is very good, with a negligible difference from the number of sub-cycles.

	A	μ	σ		A	μ	σ
300/3	3377.2	0.0	0.0715	300/3	3461.5	-3.138	11.527
300/2	2937.2	0.0	0.0781	300/2	1975.8	-3.105	12.780
150/3	1280.9	0.0	0.1709	150/3	1975.0	-15.660	17.955
150/2	1077.4	0.0	0.1783	150/2	1667.7	-15.821	18.592

Table 1. Values for amplitude A , expected value μ , variance σ in Gaussian fits shown in Figure 4 for the positions [right] and velocities [left] across simulations with different time steps. Note that we specifically fit the distribution of position differences with the expected value 0.

3.2.1 Method

To calibrate halo masses for the simulations with the reduced number of time steps, we first take all the matched halos between the 450/5 simulation and the de-tuned simulations and compute means for each mass bin. We consider only the matched halos is because the aim of the mass adjustment is to correct systematic mass differences for the halos that are theoretically identical in the different runs. After computing the means for each mass bin, we fit them to a functional form that brings the reassigned halo mass, M_{re} , close to the average halo mass for the 450/5 simulation. For our simulations, we find that the following simple form suffices for this task:

$$M_{re} = M(1.0 + \alpha(M/10^{12.0}[M_{\odot}])^{\beta}), \quad (3.1)$$

where M_{re} is the reassigned halo mass, M is the original halo mass, and α and β are free parameters. The α and β values for the simulations with different numbers of time steps are listed in Table 2 (at $z = 0.15$).

The best-fit parameters α and β are functions of redshift. For the case of the 300/2 simulation, we find best fit parameters shown below:

$$\alpha(z) = 0.123z + 0.052, \quad (3.2)$$

and

$$\beta(z) = -0.154z - 0.447. \quad (3.3)$$

	α	β
300/3	0.005	0.175
300/2	0.07	-0.47
150/3	0.101	-0.162
150/2	0.315	-0.411

Table 2. The mass reassignment parameters α and β of Eq. 3.1 for simulations run with different numbers of time steps (the results are shown at $z = 0.15$).

3.2.2 Observables

Now, we show mass functions and power spectra for the different simulations after applying the mass adjustment.

We first compute mass functions from outputs of different time-stepping schemes, as shown in Figure 5, where we compare simulations with reduced number of time steps to the 450/5 simulation at $z = 0.15$. In Figure 5, we show the ratio $n(> M)/n_{450/5}(> M)$, where $n_{450/5}(> M)$ is a cumulative mass function for the 450/5 simulation and $n(> M)$ is a cumulative mass function for different time steps shown in different colors. We compare the results before and after mass adjustment (left and right panels respectively). While the mass functions from the 250/3 and 150/2 simulations are suppressed more than 10% on all mass ranges before mass adjustment, they are significantly improved after mass adjustment, especially on halo masses greater than $10^{13.0} M_\odot$. For the simulations with the 300 global time steps, mass adjustment is especially effective on small halo masses.

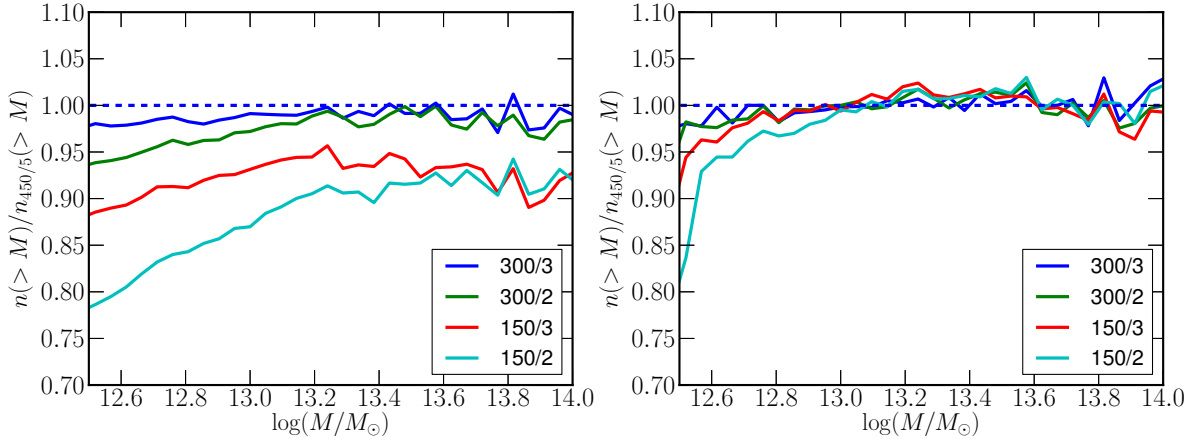


Figure 5. Comparison of cumulative mass functions in different simulations taking the 450/5 simulation as a reference. Lines, from top to bottom, correspond to the simulation with different time steps, 300/3 (blue), 300/2 (green), 150/3 (red), and 150/2 (cyan) respectively. The left panel shows the cumulative mass functions before adjusting masses (as described in the text), while the right panel is after. These plots demonstrate that a simple mass recalibration allows one to successfully recover the mass functions, even in the extreme case of the 150/2 simulation, which differed by more than 10% (on all mass scales).

The next measure of interest is halo-matter cross power spectra between halo and matter density fields, as shown in Figure 6. Figure 6 shows the ratio $P_{hm}/P_{hm,450/5}$ at $z = 0.15$, where $P_{hm,450/5}$ is the cross power spectrum for the 450/5 simulation and P_{hm} is the cross power spectrum for other time steps corresponding to different colors, as labeled in Figure 6. We use the real-space halo density field for the left panel and the redshift-space halo densities for the right panel in Figure 6. For the dark matter density field, we use the output of the 450/5 simulation for all the halo samples. Note that the dark matter density fields are in real-space for both cases. In this way, the ratio $P_{hm}/P_{hm,450/5}$ in real-space is equivalent to the ratio of halo bias between the 450/5 simulation and the simulations

with other time-steps. To select halos, we apply the soft-mass cut method using the probability given by

$$\langle N_{halo}(M) \rangle = \frac{1}{2} \text{erfc}\left(\frac{\log(M_{cut}/M)}{\sqrt{2}\sigma}\right), \quad (3.4)$$

where we set $M_{cut} = 10^{13.0} [M_{\odot}]$ and $\sigma = 0.5$. This probability has a similar form to the halo occupation distribution (hereafter, HOD) technique so that the probability gradually becomes one as increasing halo mass. We use this method to avoid noise from halos scattering across sharp boundaries on halo mass. Note that the errors calculated here are not due to sample variance, because we generate 10 samples from one full sample by using the soft-mass cut method. We see that, as we decrease the number of time steps, the ratio of the cross power spectra increases, especially in redshift-space, we observe large deviations from one on small scales for the 150/2 and 150/3 simulations. This is due to the overall smaller halo velocities for those simulations, which is shown in Figure 4. For the simulations with the 300 global time steps, overall agreements with the 450/5 simulation are almost 1% on any scales in both real-space and redshift-space.

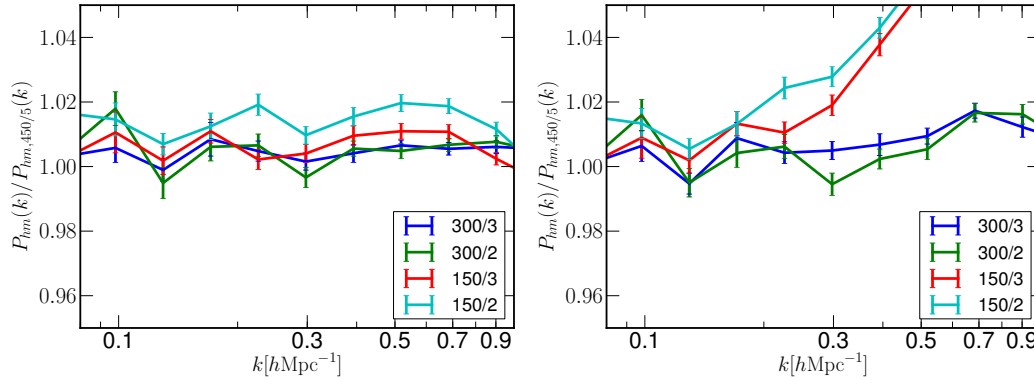


Figure 6. Ratio of halo-matter cross power spectra as a function of time steps with respect to the 450/5 simulation at $z = 0.15$. We use the real-space halo density field for the left panel and the redshift-space halo density field for the right panel, while the dark matter density fields used here are in real-space for both cases. The left panel shows that agreements with the 450/5 simulation are all within 2%. In the right panel, the large discrepancy of the cross power spectra for the simulations with 150 global steps on small scales is mainly due to the systematically small velocities, as shown in Figure 4. Note that the halos are selected based on the soft mass-cut method with $M_{cut} = 13.0$ and $\sigma = 0.5$.

As a conclusion through several convergence tests shown in this section, we find that the observables such as mass functions and power spectra are not affected by the differences on halo properties as much as those systematic differences. Based on the results in this section, we concluded that the 300/2 simulation gives sufficient resolution for halos.

4 Constructing Light Cones

We build a light cone from snapshots whose redshift range is from $z = 0.8$ to $z = 0.15$ separated constantly in redshift by $\Delta z = 0.1$. The light cone is constructed with the spherical shells. Each shell is centered at the redshift of each snapshot and has a redshift width of 0.1. In each shell, we move halo positions by using peculiar velocities to shift them into their light cone positions:

$$\vec{x}|_{z=z_{pos}} = \vec{x}|_{z=z_{snap}} + \vec{v}_{pec}|_{z=z_{snap}} \Delta t, \quad (4.1)$$

where z_{snap} is the redshift of the snapshot, z_{pos} is the redshift corresponding to its radial position, \vec{v}_{pec} is its peculiar velocity, and Δt is the time elapsed between z_{snap} and z_{pos} . For the case of a halo

crossing its boundary of the shell, we choose the halo whose distance from the boundary is closer before shifting.

To evaluate how shifting affects a spatial distribution of halos, we compare the distances for the halos at different redshift before and after shifting their positions. For the comparison, we use the halos which exist at both redshifts by matching halo particle profiles, which is the same method described in Section 3.1. Figure 7 is the histograms of distances for the matched halos at $z = 0.25$ and $z = 0.15$ before and after shifting. After shifting halos, we see that the mean distance between corresponding halos decreases from $0.4h^{-1}\text{Mpc}$ to $0.1h^{-1}\text{Mpc}$ and the standard deviation shrinks from $0.2h^{-1}\text{Mpc}$ to $0.1h^{-1}\text{Mpc}$. This result holds at all redshifts examined.

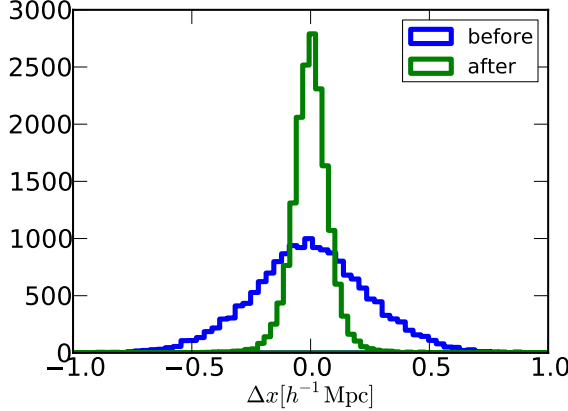


Figure 7. The histogram shown in blue is that of the distances between the position of the halos at $z = 0.25$ and where they have moved to in the simulation at $z = 0.15$. The histogram shown in green is that of the distances between the positions of the halos at $z = 0.15$, and the positions that would be predicted by shifting the positions from the $z = 0.25$ simulation assuming the peculiar velocity was constant between the snapshots (described in Eq. 4.1). The plot shows that the distances between the halos at different redshifts become smaller after the shifting.

Additionally, we compare the change in halo bias due to shifting. Figure 8 shows the ratios of halo matter cross power spectra over an auto matter power spectrum at $z = 0.15$. The plot shows that shifting halos from $z = 0.15$ to $z = 0.25$ brings down the halo bias to the one at $z = 0.25$. The agreement between the original power spectrum at $z = 0.25$ and the shifted power spectrum is 99.8% up to $1h\text{Mpc}^{-1}$. Figure 8 shows that spatial distribution of the halos is shifted to the expected distribution statistically.

A parameter when building light cones by stitching static snapshots together is how large Δz can be between various snapshots. Figure 9 test this in both real and redshift space; in redshift space, we assume the velocity of the object is unchanged between the snapshots. We see that the agreement in real space is within 1% even for the case of shifting for $\Delta z = 0.25$, while the discrepancy increases more rapidly for larger Δz in redshift space. In order to understand the cause of rapid discrepancy of the power spectra in redshift-space, we further investigate the distribution of velocity differences at different redshifts shown in Figure 10. We compare original velocities computed from the simulations in the right panel, while we multiply those velocity by the expansion factor $a(z)$ in the left panel. By scaling with the expansion factor, the velocity differences at different redshifts become smaller. Figure 11 shows the power spectra recomputed with the velocity multiplied by the ratio of $a(z)/a(z = 0.15)$, where z is the redshift of the simulation. The clustering in redshift-space is improved significantly that the overall agreement becomes within 1% on $k < 1[h\text{Mpc}^{-1}]$.

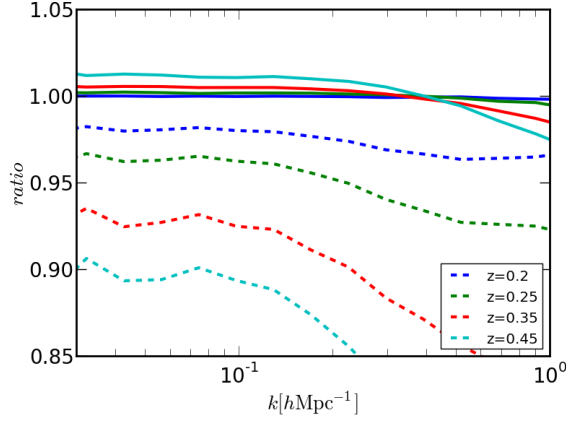


Figure 8. In this figure, we use the halo matter cross power spectra at $z = 0.25$ and $z = 0.7$ as a denominator. The dashed lines show the ratio with the cross power spectra at $z = 0.15$ and $z = 0.8$ respectively before shifting, and the solid lines are the ratio after shifting halo positions. It indicates that shifting the positions of halos from one redshift to the another preserves the distribution of halos statistically.

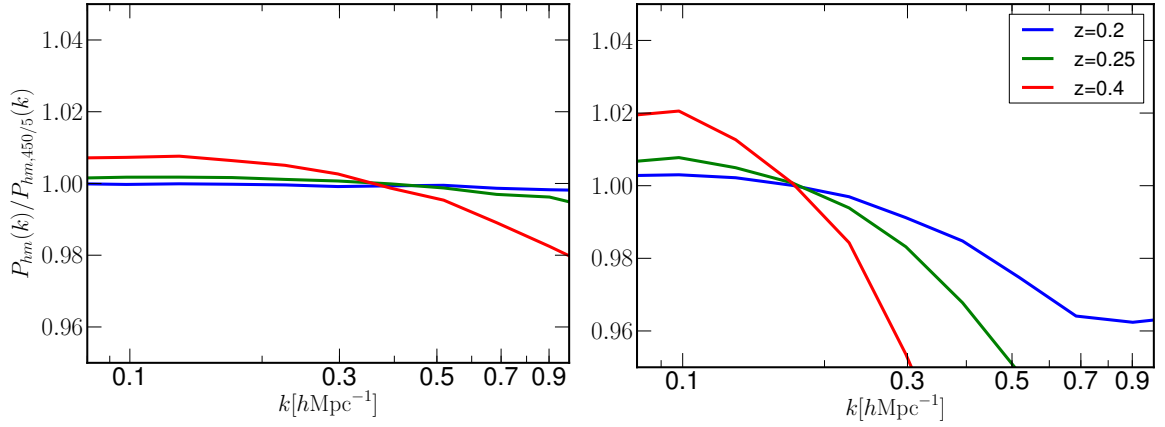


Figure 9. Ratio of halo matter cross power spectra in real space [left] and in redshift space [right] after shifting the position of the halos from the redshift labeled in the plots to $z = 0.15$. The denominator is the cross power spectra at $z = 0.15$, where we use the halo density field in real space and redshift space respectively. For all cases, we use the DM density field in real space at $z = 0.15$.

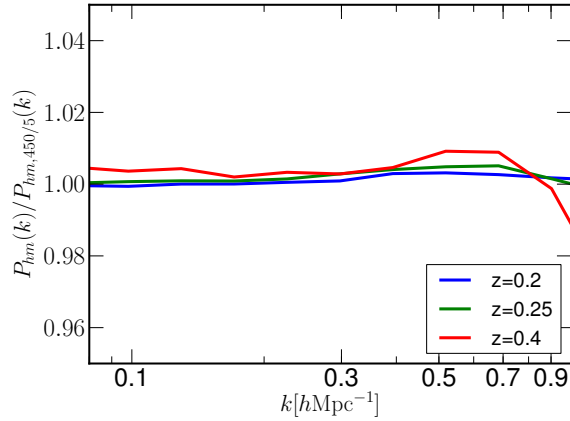


Figure 11. Ratio of halo matter cross power spectra in redshift space as shown in Figure 9. The only difference is that here we use the velocity field multiplied by the ratio of the expansion factor $a(z)/a(z = 0.15)$ (where z is the redshift shown in the figure) to compute the halo positions in redshift-space. The denominator is the cross power spectra at $z = 0.15$, where we use the halo density field in redshift space. For all cases, we use the DM density field in real space at $z = 0.15$.

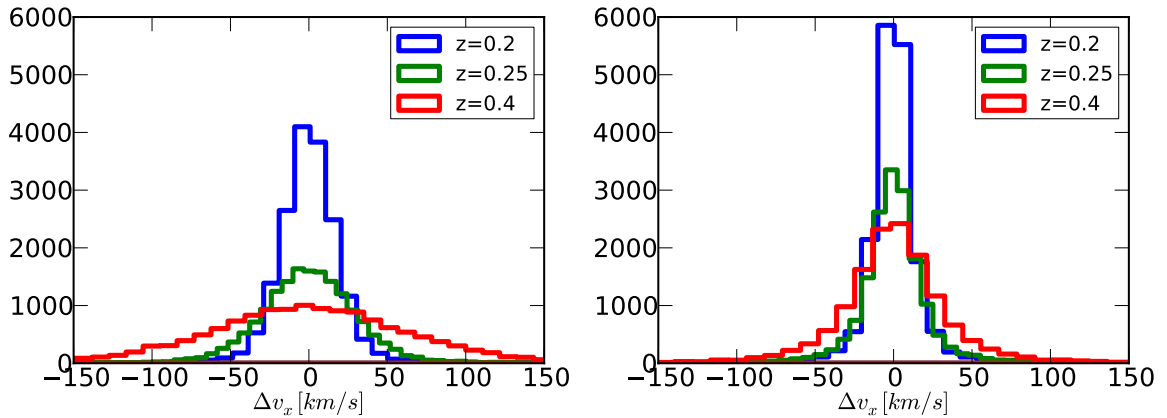


Figure 10. Comparisons of the velocities of halos matched across simulations at different redshifts to the one at $z = 0.15$. From left to right, we compare original halo velocities and the velocities multiplied by the expansion factor $a(z)$. As shown, the scatter in the velocity differences decreases in the right panel. This indicates that the change in velocities at different redshifts is largely affected by the expansion of the Universe.

5 THE BOSS SIMULATIONS

As a concrete implementation of the approach discussed above, we construct catalogs designed to mock the Baryon Oscillation Spectroscopic Survey (BOSS) galaxy samples. BOSS ([22]), part of the SDSS-III project ([23]), is a spectroscopic survey that aims to make percent level distance measurements using the baryon acoustic oscillation technique. The low redshift ($z < 0.7$) distance measurements use two galaxy samples: the LOWZ ($z < 0.45$) and CMASS ($z < 0.7$) samples ([24, 25]). We focus on the CMASS sample below; however, the same halo catalogs are useful for the LOWZ sample as well.

We choose a simulation volume large enough to build a full-sky mock BOSS catalog. Since the CMASS sample extends to $z \sim 0.7$, we choose a simulation side of $4000h^{-1}\text{Mpc}$, corresponding to a comoving distance to $z \sim 0.8$ from the center of the box; Fig. 12 shows the BOSS CMASS

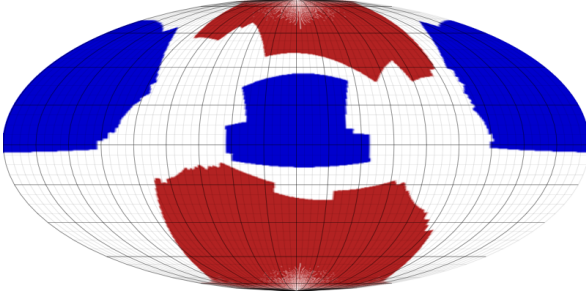


Figure 12. Demonstrating how we fit two non-overlapping BOSS volumes into the same simulation box. The blue region is the BOSS survey footprint in equatorial coordinates, while the red region is the same region rotated using the rotation matrix given in the text.

redshift distribution as a function of redshift and comoving distance (assuming our fiducial cosmology). Our simulations are run with 4000^3 particles, corresponding to a particle mass of $10^{11}M_\odot$. The characteristic halo mass for BOSS galaxies corresponds to $10^{13}M_\odot$, which we resolve with 100 particles. We keep all halos down to 40 particles corresponding to a halo mass of $10^{12.6}M_\odot$. The simulations are started at $z = 200$ with Zel’dovich initial conditions and are stopped at $z = 0.15$ with simulation outputs every $\Delta z = 0.05$. At each of these steps, we store XXX.

The BOSS angular geometry is split into two regions : one in the North Galactic Cap and one in the South Galactic Cap (Fig. 12). Since we generate full-sky mocks, it is straightforward to embed two full non-overlapping BOSS surveys in a single mock realization (Fig. 12). We cut out a first BOSS volume with \vec{x}_{old} and then define a new coordinate system \vec{x}_{new} such as $\vec{x}_{new} = R\vec{x}_{old}$, where R is the Euler rotation matrix for Fig. 12:

$$R = \begin{pmatrix} 0.088 & 0.096 & 0.991 \\ 0.219 & -0.973 & 0.075 \\ 0.972 & 0.211 & -0.107 \end{pmatrix}.$$

5.1 Building the Galaxy Catalog

To generate galaxy mock catalogs, we need to go through the following steps:

- 1) populate halos with galaxies through the HOD functional form,
- 2) give positions and velocities to the galaxies assuming an NFW profile [26].

The HOD functional form gives probabilities for the number of central and satellite galaxies based on mass of halos which host those galaxies with five free parameters. A halo hosts a central galaxy with probability $N_{cen}(M)$ and a number of satellite galaxies given by a Poisson distribution with mean $N_{sat}(M)$:

$$N_{cen}(M) = \frac{1}{2} \operatorname{erfc} \left[\frac{\ln(M_{cut}/M)}{\sqrt{2}\sigma} \right], \quad (5.1)$$

and

$$N_{sat}(M) = N_{cen}(M) \left(\frac{M - \kappa M_{cut}}{M_1} \right)^\alpha, \quad (5.2)$$

where M_{cut} , M_1 , σ , κ , and α are free parameters and M is the halo mass. We assume that $N_{sat}(M)$ is zero when $M < \kappa M_{cut}$ and halos do not host satellite galaxies without a central galaxy ([27]). The total number of galaxies hosted by each halo is a sum of the number of central and satellite galaxies. Eqs 5.1 and 5.2 are not the only possible functional form for the HOD, and it is trivial to change this. However, these forms reproduce the clustering of the BOSS galaxies ([28]) and we use them in what follows.

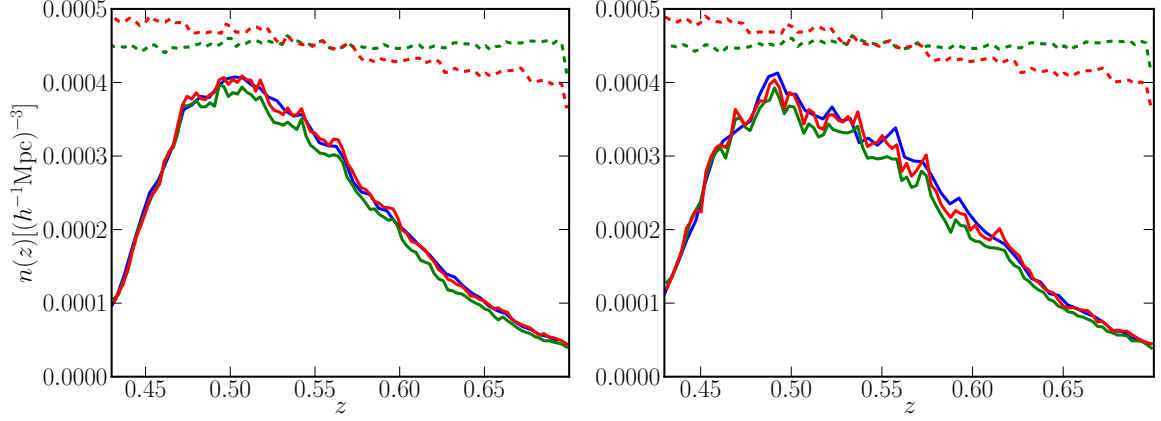


Figure 13. A comparison of galaxy number densities before fitting to DR11 [dashed lines] and after [solid lines]. The blue solid line is $n(z)$ from DR11 (North) in [30]. The green and red lines are from the mocks at $z = 0.55$ and the lightcone output respectively. The HOD parameters used to generate the mock catalogs can be found in text.

We place the central galaxies at the center, with a velocity equal to the halo velocity. We distribute satellite galaxies with an spherically symmetric NFW profile:

$$\rho(r) = \frac{4\rho_s}{\frac{cr}{R_{vir}}(1 + \frac{cr}{R_{vir}})^2}, \quad (5.3)$$

where ρ_s is the density at the characteristic scale $r_s = R_{vir}/c$, R_{vir} is the virial radius for the halo and c determines how centrally concentrated the profile is. R_{vir} is computed from $M = \frac{4\pi}{3}R_{vir}^3\rho_{crit}\Delta_h$, where $\Delta_h = (18\pi^2 + 82(\Omega_m - 1) - 39(\Omega_m - 1)^2)/\Omega_m$ and $\rho_{crit} = \frac{3c^2 H_0^2}{8\pi G}$ (c is the speed of light here). We adopt the form in [29]:

$$c(M, z) = \frac{c_0}{1+z}(M/M_0)^{-\beta}, \quad (5.4)$$

where $c_0 = 9.60$, $M_0 = 10^{12}$, and $\beta = 0.075$. There have been several studies about concentration, those different expressions on concentration do not make difference for our purpose.

The velocities of the satellite galaxies are the sum of their host halo velocity and a random virial component. This random component are given as follows:

$$\langle v_x^2 \rangle = \langle v_y^2 \rangle = \langle v_z^2 \rangle = \frac{1}{3} \frac{GM}{R_{vir}}. \quad (5.5)$$

We draw a Gaussian distribution with zero mean and variance in Eq. 5.5 to give each component of an internal velocity for the satellite galaxies. Here, we assume that satellite galaxies are randomly moving inside the host halos. So, we give the radial component of this random motion from the Gaussian distribution and determine the direction randomly with equal probability.

We generate galaxy mocks from the static snapshots at $z = 0.55$. In Figure 14, we compare the correlations function $\xi(s)$ with the one in [30], where s is the separation in redshift-space. Here, we use the following HOD parameters, $M_{cut} = 12.9$, $\alpha = 1.013$, $\kappa = 1.0$, $\sigma = 0.85$.

Note that we fit the average number density of galaxies to that of [30] as shown in Figure 13. In order to fit the number density, we randomly select galaxies after populating halos through HOD.

The correlation function computed from our sample mocks fits to the correlation function in [30] well on the scale between $30h^{-1}\text{Mpc}$ and $80h^{-1}\text{Mpc}$ shown in Figure 14. We compute χ^2 for monopoles and quadrupoles from the simulation at $z = 0.55$ and the light cone output. We obtain $\chi^2 = 23.4$ for the simulation at $z = 0.55$ and $\chi^2 = 25.0$ for the light cone output. The degree of freedom here is 14 where $s \in [30h^{-1}\text{Mpc}, 78h^{-1}\text{Mpc}]$.

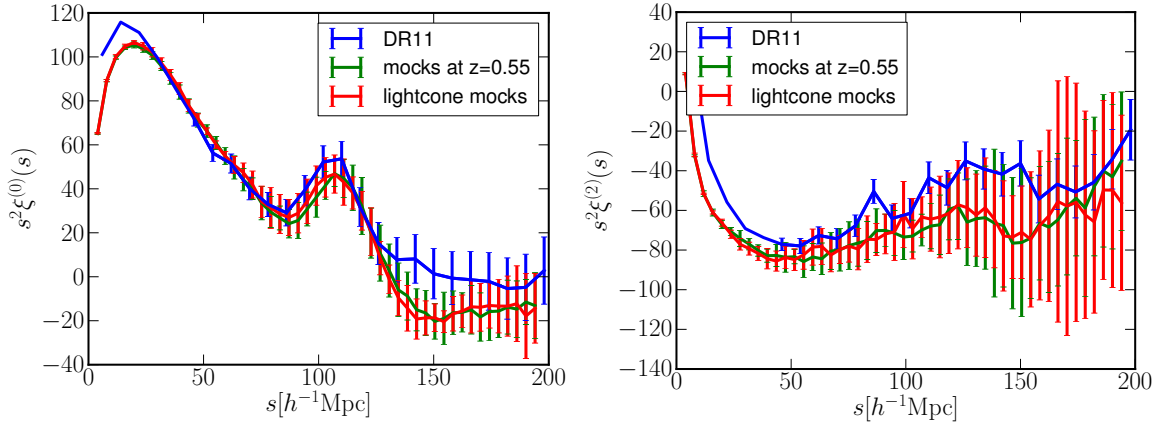


Figure 14. Correlation function monopoles $\xi^{(0)}(s)$ [left] and quadrupoles $\xi^{(2)}(s)$ [right] of the mocks (green) and DR11 in [13] (blue) at $z = 0.55$. The HOD parameters used to generate the mock catalogs can be found in text.

6 Discussion

Precision required for current and future galaxy spectroscopic surveys to test the expansion and structure formation histories of the Universe requires an accurate understanding of systematic effects. In this paper we have presented a quantitative study of the impact of time step sizes on the halo and matter density fields. Our code has two adjustable time stepping parameters - a global time step and a number of sub-cycles (responsible for a particle-particle interactions) to track that particle trajectories on small scales. We consider cases where we increase the length of each time step by factors of 1.5 and 3 respectively, as well as reducing the number of sub-cycles. Our fiducial choice is to use using 300 global time steps corresponding to $\Delta a(z) = 0.003$ and 2 sub-cycles (increasing the length of the global time step by a factor of 1.5 and that of the sub-cycles by a factor of 2.5), resulting in a reduction of the simulation run time by 4 times less. We keep the mass resolution constant; the results here are based on a particle mass of $6.86 \times 10^{10} h M_{\odot}$. We summarize the key results below:

(a) The halo masses tend to be underestimated in these cases, as one might expect because reducing the number of time steps produces halos with less substructure and a more diffuse distribution of mass. However, this trend may be calibrated with smaller simulations and corrected, recovering the halo masses to 98%. The halo mass function is correctly recovered fully for masses above $10^{12.7} h^{-1} M_{\odot}$ corresponding to 100 particles. Note that we run the halo finder with identical parameters as in the full resolution runs. It may however be possible to get similar results by changing the parameters of the halo finder, as was done in [13].

(b) The halo positions and velocities are recovered with a scatter of $0.08 [h^{-1} \text{Mpc}]$ and $12.8 [\text{km/s}]$ respectively for the simulation of our fiducial choice.

(c) The clustering of these halos is correctly recovered to better than 1% on scales below $k < 1 [h \text{Mpc}^{-1}]$ in real-space and $k < 0.5 [h \text{Mpc}^{-1}]$.

(d) We find that the number of sub-cycles makes almost no difference to any of our final results.

We also consider the redshift sampling required to construct light cone outputs. We first compare the distances for the halos at different redshifts before and after shifting their positions from one redshift to the another. Moving halos over a $\Delta z = 0.1$ interval correctly reduces the standard deviation of those distances from $0.25 [h^{-1} \text{Mpc}]$ to $0.09 [h^{-1} \text{Mpc}]$. Moreover, the power spectra are correctly recovered to better than 1% for $k < 0.5 [h \text{Mpc}^{-1}]$ for $\Delta z = 0.25$. This worsens in redshift space to 2% up to $k < 0.2 [h \text{Mpc}^{-1}]$. The agreement is, however, improved to 1% for $k < 1 [h \text{Mpc}^{-1}]$ by using the velocity scaled by the relative scale factor between the snapshot and the true redshift. Our fiducial choice to construct light cone outputs is $\Delta z = 0.05$.

This work is a natural extension of the approaches described in [7, 11–14]. The primary goal

for those papers was to generate the large numbers of simulations required for estimating covariance matrices. We quantify, in detail, the impact of size of the time step on large scale observables; our suite of simulations are better designed for testing for systematic errors in theory and analysis techniques. As a proof of principle, we present a set of eight full BOSS (both North and South Galactic caps simultaneously) simulations. The time savings presented in this paper allowed to extend this to 50 simulations, across a range of cosmologies. These results from these will be presented in future publications.

Acknowledgement

TS and NP are supported by a DOE Early Career Grant. This work was supported in part by the facilities and staff of the Yale University Faculty of Arts and Sciences High Performance Computing Center, and by resources at the National Energy Research Scientific Computing Center. TS would like to thank Andrew Szymakowski for useful discussions. This research used resources of the National Energy Research Scientific Computing Center, a DOE Office of Science User Facility supported by the Office of Science of the U.S. Department of Energy under Contract No. DE-AC02-05CH11231. Argonne National Laboratory’s work was supported under U.S. Department of Energy contract DE-AC02-06CH11357.

References

- [1] P. Monaco, T. Theuns, G. Taffoni, F. Governato, T. Quinn, and J. Stadel, *Predicting the Number, Spatial Distribution, and Merging History of Dark Matter Halos*, *ApJ* **564** (Jan., 2002) 8–14, [[astro-ph/0109322](#)].
- [2] P. Monaco, T. Theuns, and G. Taffoni, *The pinocchio algorithm: pinpointing orbit-crossing collapsed hierarchical objects in a linear density field*, *MNRAS* **331** (Apr., 2002) 587–608, [[astro-ph/0109323](#)].
- [3] P. Fosalba, E. Gaztañaga, F. J. Castander, and M. Manera, *The onion universe: all sky lightcone simulations in spherical shells*, *MNRAS* **391** (Nov., 2008) 435–446, [[arXiv:0711.1540](#)].
- [4] K. Riebe, A. M. Partl, H. Enke, J. Forero-Romero, S. Gottlöber, A. Klypin, G. Lemson, F. Prada, J. R. Primack, M. Steinmetz, and V. Turchaninov, *The MultiDark Database: Release of the Bolshoi and MultiDark cosmological simulations*, *Astronomische Nachrichten* **334** (Aug., 2013) 691–708.
- [5] M. Crocce, F. J. Castander, E. Gaztanaga, P. Fosalba, and J. Carretero, *The MICE Grand Challenge Lightcone Simulation II: Halo and Galaxy catalogues*, *ArXiv e-prints* (Dec., 2013) [[arXiv:1312.2013](#)].
- [6] S. Tashev, M. Zaldarriaga, and D. J. Eisenstein, *Solving large scale structure in ten easy steps with COLA*, *JCAP* **6** (June, 2013) 36, [[arXiv:1301.0322](#)].
- [7] M. White, J. L. Tinker, and C. K. McBride, *Mock galaxy catalogues using the quick particle mesh method*, *MNRAS* **437** (Jan., 2014) 2594–2606, [[arXiv:1309.5532](#)].
- [8] P. Monaco, E. Sefusatti, S. Borgani, M. Crocce, P. Fosalba, R. K. Sheth, and T. Theuns, *An accurate tool for the fast generation of dark matter halo catalogues*, *MNRAS* **433** (Aug., 2013) 2389–2402, [[arXiv:1305.1505](#)].
- [9] T. Hamana, S. Colombi, and Y. Suto, *Two-point correlation functions on the light cone: Testing theoretical predictions against N-body simulations*, *A&A* **367** (Feb., 2001) 18–26, [[astro-ph/0010287](#)].
- [10] M. Sato, T. Hamana, R. Takahashi, M. Takada, N. Yoshida, T. Matsubara, and N. Sugiyama, *Simulations of Wide-Field Weak Lensing Surveys. I. Basic Statistics and Non-Gaussian Effects*, *ApJ* **701** (Aug., 2009) 945–954, [[arXiv:0906.2237](#)].
- [11] F.-S. Kitaura, G. Yepes, and F. Prada, *Modelling baryon acoustic oscillations with perturbation theory and stochastic halo biasing*, *MNRAS* **439** (Mar., 2014) L21–L25, [[arXiv:1307.3285](#)].
- [12] C.-H. Chuang, F.-S. Kitaura, F. Prada, C. Zhao, and G. Yepes, *EZmocks: extending the Zel’dovich approximation to generate mock galaxy catalogues with accurate clustering statistics*, *ArXiv e-prints* (Sept., 2014) [[arXiv:1409.1124](#)].

- [13] M. Manera, R. Scoccimarro, W. J. Percival, L. Samushia, C. K. McBride, A. J. Ross, R. K. Sheth, M. White, B. A. Reid, A. G. Sánchez, R. de Putter, X. Xu, A. A. Berlind, J. Brinkmann, C. Maraston, B. Nichol, F. Montesano, N. Padmanabhan, R. A. Skibba, R. Tojeiro, and B. A. Weaver, *The clustering of galaxies in the SDSS-III Baryon Oscillation Spectroscopic Survey: a large sample of mock galaxy catalogues*, MNRAS **428** (Jan., 2013) 1036–1054, [[arXiv:1203.6609](#)].
- [14] M. Manera, L. Samushia, R. Tojeiro, C. Howlett, A. J. Ross, W. J. Percival, H. Gil-Marín, J. R. Brownstein, A. Burden, and F. Montesano, *The clustering of galaxies in the SDSS-III Baryon Oscillation Spectroscopic Survey: mock galaxy catalogues for the low-redshift sample*, *ArXiv e-prints* (Jan., 2014) [[arXiv:1401.4171](#)].
- [15] S. Habib, A. Pope, L. Lukić, D. Daniel, P. Fasel, N. Desai, K. Heitmann, C.-H. Chuang, L. Ankeny, G. Mark, S. Bhattacharya, and J. Ahrens, *Hybrid petacomputing meets cosmology: The roadrunner universe project*, *Journal of Physics: Conference Series* **180** (2009), no. 1 012019.
- [16] A. Pope, S. Habib, Z. Lukic, D. Daniel, P. Fasel, N. Desai, and K. Heitmann, *The accelerated universe*, *Computing in Science and Engg.* **12** (July, 2010) 17–25.
- [17] S. Habib, V. Morozov, H. Finkel, A. Pope, K. Heitmann, K. Kumaran, T. Peterka, J. Insley, D. Daniel, P. Fasel, N. Frontiere, and Z. Lukic, *The Universe at Extreme Scale: Multi-Petaflop Sky Simulation on the BG/Q*, *ArXiv e-prints* (Nov., 2012) [[arXiv:1211.4864](#)].
- [18] M. White, A. Pope, J. Carlson, K. Heitmann, S. Habib, P. Fasel, D. Daniel, and Z. Lukic, *Particle Mesh Simulations of the Ly α Forest and the Signature of Baryon Acoustic Oscillations in the Intergalactic Medium*, ApJ **713** (Apr., 2010) 383–393, [[arXiv:0911.5341](#)].
- [19] S. Bhattacharya, S. Habib, K. Heitmann, and A. Vikhlinin, *Dark Matter Halo Profiles of Massive Clusters: Theory versus Observations*, ApJ **766** (Mar., 2013) 32, [[arXiv:1112.5479](#)].
- [20] R. W. Hockney and J. W. Eastwood, *Computer simulation using particles*. 1988.
- [21] K. Heitmann, P. M. Ricker, M. S. Warren, and S. Habib, *Robustness of Cosmological Simulations. I. Large-Scale Structure*, ApJS **160** (Sept., 2005) 28–58, [[astro-ph/0411795](#)].
- [22] K. S. Dawson, D. J. Schlegel, C. P. Ahn, S. F. Anderson, É. Aubourg, S. Bailey, R. H. Barkhouser, J. E. Bautista, A. Beifiori, A. A. Berlind, V. Bhardwaj, D. Bizyaev, C. H. Blake, M. R. Blanton, M. Blomqvist, A. S. Bolton, A. Borde, J. Bovy, W. N. Brandt, H. Brewington, J. Brinkmann, P. J. Brown, J. R. Brownstein, K. Bundy, N. G. Busca, W. Carithers, A. R. Carnero, M. A. Carr, Y. Chen, J. Comparat, N. Connolly, F. Cope, R. A. C. Croft, A. J. Cuesta, L. N. da Costa, J. R. A. Davenport, T. Delubac, R. de Putter, S. Dhital, A. Ealet, G. L. Ebelke, D. J. Eisenstein, S. Escoffier, X. Fan, N. Filiz Ak, H. Finley, A. Font-Ribera, R. Génova-Santos, J. E. Gunn, H. Guo, D. Haggard, P. B. Hall, J.-C. Hamilton, B. Harris, D. W. Harris, S. Ho, D. W. Hogg, D. Holder, K. Honscheid, J. Huehnerhoff, B. Jordan, W. P. Jordan, G. Kauffmann, E. A. Kazin, D. Kirkby, M. A. Klaene, J.-P. Kneib, J.-M. Le Goff, K.-G. Lee, D. C. Long, C. P. Loomis, B. Lundgren, R. H. Lupton, M. A. G. Maia, M. Makler, E. Malanushenko, V. Malanushenko, R. Mandelbaum, M. Manera, C. Maraston, D. Margala, K. L. Masters, C. K. McBride, P. McDonald, I. D. McGreer, R. G. McMahon, O. Mena, J. Miralda-Escudé, A. D. Montero-Dorta, F. Montesano, D. Muna, A. D. Myers, T. Naugle, R. C. Nichol, P. Noterdaeme, S. E. Nuza, M. D. Olmstead, A. Oravetz, D. J. Oravetz, R. Owen, N. Padmanabhan, N. Palanque-Delabrouille, K. Pan, J. K. Parejko, I. Pâris, W. J. Percival, I. Pérez-Fournon, I. Pérez-Ràfols, P. Petitjean, R. Pfaffenberger, J. Pforr, M. M. Pieri, F. Prada, A. M. Price-Whelan, M. J. Raddick, R. Rebolo, J. Rich, G. T. Richards, C. M. Rockosi, N. A. Roe, A. J. Ross, N. P. Ross, G. Rossi, J. A. Rubiño-Martín, L. Samushia, A. G. Sánchez, C. Sayres, S. J. Schmidt, D. P. Schneider, C. G. Scóccola, H.-J. Seo, A. Shelden, E. Sheldon, Y. Shen, Y. Shu, A. Slosar, S. A. Smee, S. A. Snedden, F. Stauffer, O. Steele, M. A. Strauss, A. Streblyanska, N. Suzuki, M. E. C. Swanson, T. Tal, M. Tanaka, D. Thomas, J. L. Tinker, R. Tojeiro, C. A. Tremonti, M. Vargas Magaña, L. Verde, M. Viel, D. A. Wake, M. Watson, B. A. Weaver, D. H. Weinberg, B. J. Weiner, A. A. West, M. White, W. M. Wood-Vasey, C. Yeche, I. Zehavi, G.-B. Zhao, and Z. Zheng, *The Baryon Oscillation Spectroscopic Survey of SDSS-III*, AJ **145** (Jan., 2013) 10, [[arXiv:1208.0022](#)].
- [23] D. J. Eisenstein, D. H. Weinberg, E. Agol, H. Aihara, C. Allende Prieto, S. F. Anderson, J. A. Arns, É. Aubourg, S. Bailey, E. Balbinot, and et al., *SDSS-III: Massive Spectroscopic Surveys of the Distant Universe, the Milky Way, and Extra-Solar Planetary Systems*, AJ **142** (Sept., 2011) 72, [[arXiv:1101.1529](#)].

- [24] L. Anderson, É. Aubourg, S. Bailey, F. Beutler, V. Bhardwaj, M. Blanton, A. S. Bolton, J. Brinkmann, J. R. Brownstein, A. Burden, C.-H. Chuang, A. J. Cuesta, K. S. Dawson, D. J. Eisenstein, S. Escoffier, J. E. Gunn, H. Guo, S. Ho, K. Honscheid, C. Howlett, D. Kirkby, R. H. Lupton, M. Manera, C. Maraston, C. K. McBride, O. Mena, F. Montesano, R. C. Nichol, S. E. Nuza, M. D. Olmstead, N. Padmanabhan, N. Palanque-Delabrouille, J. Parejko, W. J. Percival, P. Petitjean, F. Prada, A. M. Price-Whelan, B. Reid, N. A. Roe, A. J. Ross, N. P. Ross, C. G. Sabiu, S. Saito, L. Samushia, A. G. Sánchez, D. J. Schlegel, D. P. Schneider, C. G. Scoccola, H.-J. Seo, R. A. Skibba, M. A. Strauss, M. E. C. Swanson, D. Thomas, J. L. Tinker, R. Tojeiro, M. V. Magaña, L. Verde, D. A. Wake, B. A. Weaver, D. H. Weinberg, M. White, X. Xu, C. Yèche, I. Zehavi, and G.-B. Zhao, *The clustering of galaxies in the SDSS-III Baryon Oscillation Spectroscopic Survey: baryon acoustic oscillations in the Data Releases 10 and 11 Galaxy samples*, MNRAS **441** (June, 2014) 24–62, [[arXiv:1312.4877](#)].
- [25] R. Tojeiro, A. J. Ross, A. Burden, L. Samushia, M. Manera, W. J. Percival, F. Beutler, J. Brinkmann, J. R. Brownstein, A. J. Cuesta, K. Dawson, D. J. Eisenstein, S. Ho, C. Howlett, C. K. McBride, F. Montesano, M. D. Olmstead, J. K. Parejko, B. Reid, A. G. Sánchez, D. J. Schlegel, D. P. Schneider, J. L. Tinker, M. V. Magaña, and M. White, *The clustering of galaxies in the SDSS-III Baryon Oscillation Spectroscopic Survey: galaxy clustering measurements in the low-redshift sample of Data Release 11*, MNRAS **440** (May, 2014) 2222–2237, [[arXiv:1401.1768](#)].
- [26] J. F. Navarro, C. S. Frenk, and S. D. M. White, *The Structure of Cold Dark Matter Halos*, ApJ **462** (May, 1996) 563, [[astro-ph/9508025](#)].
- [27] Z. Zheng, A. A. Berlind, D. H. Weinberg, A. J. Benson, C. M. Baugh, S. Cole, R. Davé, C. S. Frenk, N. Katz, and C. G. Lacey, *Theoretical Models of the Halo Occupation Distribution: Separating Central and Satellite Galaxies*, ApJ **633** (Nov., 2005) 791–809, [[astro-ph/0408564](#)].
- [28] M. White, M. Blanton, A. Bolton, D. Schlegel, J. Tinker, A. Berlind, L. da Costa, E. Kazin, Y.-T. Lin, M. Maia, C. K. McBride, N. Padmanabhan, J. Parejko, W. Percival, F. Prada, B. Ramos, E. Sheldon, F. de Simoni, R. Skibba, D. Thomas, D. Wake, I. Zehavi, Z. Zheng, R. Nichol, D. P. Schneider, M. A. Strauss, B. A. Weaver, and D. H. Weinberg, *The Clustering of Massive Galaxies at $z \sim 0.5$ from the First Semester of BOSS Data*, ApJ **728** (Feb., 2011) 126, [[arXiv:1010.4915](#)].
- [29] A. A. Klypin, S. Trujillo-Gomez, and J. Primack, *Dark Matter Halos in the Standard Cosmological Model: Results from the Bolshoi Simulation*, ApJ **740** (Oct., 2011) 102, [[arXiv:1002.3660](#)].
- [30] L. Anderson, E. Aubourg, S. Bailey, F. Beutler, A. S. Bolton, J. Brinkmann, J. R. Brownstein, C.-H. Chuang, A. J. Cuesta, K. S. Dawson, D. J. Eisenstein, K. Honscheid, E. A. Kazin, D. Kirkby, M. Manera, C. K. McBride, O. Mena, R. C. Nichol, M. D. Olmstead, N. Padmanabhan, N. Palanque-Delabrouille, W. J. Percival, F. Prada, A. J. Ross, N. P. Ross, A. G. Sanchez, L. Samushia, D. J. Schlegel, D. P. Schneider, H.-J. Seo, M. A. Strauss, D. Thomas, J. L. Tinker, R. Tojeiro, L. Verde, D. H. Weinberg, X. Xu, and C. Yèche, *The clustering of galaxies in the SDSS-III Baryon Oscillation Spectroscopic Survey: Measuring D_A and H at $z=0.57$ from the Baryon Acoustic Peak in the Data Release 9 Spectroscopic Galaxy Sample*, ArXiv e-prints (Mar., 2013) [[arXiv:1303.4666](#)].